

FAILURE AND FRAGMENTATION OF METEORITES AND BASALT: UNDERSTANDING LUNAR REGOLITH GENERATION J. D. Hogan¹, J. Plescia², and K. T. Ramesh¹, ¹Hopkins Extreme Materials Institute, The Johns Hopkins University, Baltimore, Maryland 21218, ²Applied Physics Laboratory, The Johns Hopkins University, Laurel, Maryland 20723

Introduction: Understanding the behavior of planetary materials in extreme loading conditions is central in interpreting planetary impacts [1] and collisions between asteroids [2]. Planetary materials are comprised of mineral and metal grains and amorphous clasts, each with varying properties, shapes and sizes. During impact events, the bodies will experience a range of deformation rates (units: s^{-1}) and stress states (e.g., compression, tension, shear). Failure during impact occurs predominately in compression, with local tensile regions near free surfaces. The complex loading history and the mineral phases dictate the degree of intergranular (along grain boundaries) and transgranular (through grains) fracture.

The coalescence of fractures results in a wide range of fragment sizes, and these fragment size distributions can offer insight into important physical processes. The size-frequency distributions of larger fragments (boulders) on Eros [3] have been used to constrain its collisional history. For smaller fragments, interests exists in understanding regolith generation and in excavation and processing [1,4]; important areas in the development of lunar colonies. In this study, we investigate failure and fragmentation of a meteorite (an L6 chondrite) and basalt for loading rates of $10^{-3}s^{-1}$ (MTS machine) and $10^{+3}s^{-1}$ (Kolsky bar) [5]. These are representative materials of asteroids and the Moon. Image processing is used to measure the size and shape distributions of the fragments. Distributions are linked to the microstructure. Mass-size distributions are then compared with lunar regolith samples from Apollo 17 [6].

Meteorite, Basalt and Regolith Materials: The meteorite is GRO 85209, an L6 chondrite consisting primarily of olivine (25% Fa), low-Ca pyroxene (21% Fs), and iron nickel [7]; olivine ($>200\ \mu\text{m}$ and circular), pyroxene ($<500\ \mu\text{m}$ and darker in shade), and iron nickel (black in color) are shown in Fig 1a. Analysis of the thin sections (Fig. 1a) indicates there are no major fractures, shock veins or brecciation. Iron nickel occurs as blocky grains throughout. Large olivine grains show only irregular fractures and no undulatory extinction, suggesting a shock stage of S1. The basalt was purchased from Coverall Stone, WA and is comprised of 55% plagioclase, 25% olivine, and 20% clinopyroxene. Apollo 17 sample 78481, 27 is a shallow surface sample ($<1\ \text{cm}$ depth) from a trench at Station 8 at the base of Sculptured Hills. The material has an I_s/FeO of 82 and it is mature.

Results: Cumulative distributions of principal axis sizes (taken as the fragment's longest spanning dimension) for GRO 85209 are examined in Fig. 2a. There are 147,323 ($10^{-3}\ s^{-1}$ test) and 433,561 ($10^3\ s^{-1}$ test) fragments and the median fragment size is $\sim 5.7\ \mu\text{m}$ for both cases. The distributions overlap between 4 and 9 μm and this makes up approximately 90% of the total fragment number. There appears to be two distinct size distributions that are separated at $\sim 30\ \mu\text{m}$. Also shown in the figure is the distribution of spacing's between neighboring metal grains. Changes in this curve occur for sizes $>10\ \mu\text{m}$ and $>40\ \mu\text{m}$.

Plotted in Fig. 2b is the fragment circularity (defined as: $(2\pi A)^{0.5}/P$, where A is projected area and P is the fragment perimeter) against principal axis size. Blocky fragments have lower circularities. Three regions are highlighted: **I.** circularities of 0.2 to 1, sizes $<30\ \mu\text{m}$; **II.** circularities 0.5 to 1.2, all sizes; **III.** circularity >0.8 , sizes $>300\ \mu\text{m}$. These regions will be correlated with images of the microstructure and fragments in Fig. 1. Fig. 1b illustrates the fracture patterns in the silicate grain; the fragment is $>1\ \text{mm}$, non-circular and contains multiple fractures. Fractures appear to originate/intersect at regions of high angularity on the metal grains. This is consistent with exposed iron nickel grains on fragment surfaces (Fig. 1b-d). Figure 1c illustrates typical shapes for sub- $100\ \mu\text{m}$ (Fig. 1c) and sub- $500\ \mu\text{m}$ (Fig. 1d) fragments. Fragments are primarily comprised of pyroxene, with some individual metal grains. The highly fractured fragment in Fig 1b is also likely pyroxene

Discussion and Implications: The compressive failure of brittle materials is typically described by the wing-crack mechanism [8]. During loading, cracks initiate from stress concentrations (e.g., flaws) and will grow in a stable manner in response to the local stress state. In GRO 85029, fracture is believed to be initiated at metal grains in regions of high angularity. As loading continues, internal fractures accumulate and the material will continue to absorb strain energy, and kinetic energy under dynamic loading, until a critical number of flaws have coalesced. At this point the peak stress (i.e., compressive strength) is reached and the material begins to lose its load-carrying capacity. It has been shown in transparent materials that the number of fractures accumulated at peak stress are relatively few in comparison to those that form after peak stress [9].

During unloading, the energy is released as a free expansion process, tensile stresses are created and fragmentation ensues via unstable crack growth. Multiple fragment types may be formed during unloading (Fig. 2b). Region I comprises of pyroxene, are $<30 \mu\text{m}$ (median $5.7 \mu\text{m}$) and represent $>85\%$ of the total population. In Region II, the majority of fragments are polyphase (metal and pyroxene in Fig. 1b) and polygrain (dominated by pyroxene). Fragments are formed from coalesced fractures between neighboring metal grains. Region III is believed to be comprised of olivine grains because of their higher circularity.

Comparison with Lunar Regolith: In this study, the generation of $>100\text{K}$ sub- $30 \mu\text{m}$ fragments has been shown to be a consequence of compressive failure. With this in mind, mass-size fragment distributions of lunar regolith sample 78481, 27 are compared with GRO 85209 and basalt (Fig. 3). Sizes corresponding to 50% of the mass are $60 \mu\text{m}$ for sample 78481, 27, $232 \mu\text{m}$ for GRO 85209, and $913 \mu\text{m}$ for basalt. By this metric, the regolith is 4 times more crushed than the meteorite and 15 times more crushed than the basalt. Significantly more fines for the regolith sample is likely associated with erosion, thermal fragmentation, and continual bombardment. The differences between meteorite and basalt may have implications for the use of terrestrial basalt as a simulant for meteorite material. In basalt, fracture originating from olivine grains (like metal in the meteorite) dominates its mass-size distribution for $>150 \mu\text{m}$. Basalt also has twice the compressive strength of GRO 85029.

Concluding Remarks: The effect of microstructure on the compressive failure and fragmentation of planetary materials was examined. Microstructure-dependent fragment types were observed and mechanisms governing the generation of small and large fragments were discussed. On-going work is needed to bridge lunar regolith measurements with experiments. For example, experiments could be conducted on pre-fragmented samples to observe further comminution.

References: [1] Horz F. and Cintala M. (1997), *Meteoritics & Planet. Sci.*, 32, 179-209. [2] Michel P. et al. (2003), *Nature*, 421, 608-611. [3] Dombard A. J. et al. (2010), *Icarus*, 210, 713-721. [4] Landis G. A. (2007), *Acta Astronautica*, 60, 906-915. [5] Stickle A.M. et al. (2013), *LPS XLIV*, Abstract #1719. [6] Graf J. C. (1993), *NASA Ref. Pub.*, 1265, 466 pp. [7] Grossman J. N. (1994), *Meteoritics & Planet. Sci.*, 29, 100-143. [8] Nemmet-Nasser S. and Horii H. (1982), *JGR*, 87, B8, 6805-6821. [9] Hu G. et al. (2011), *JMPS*, 59, 1076-1093.

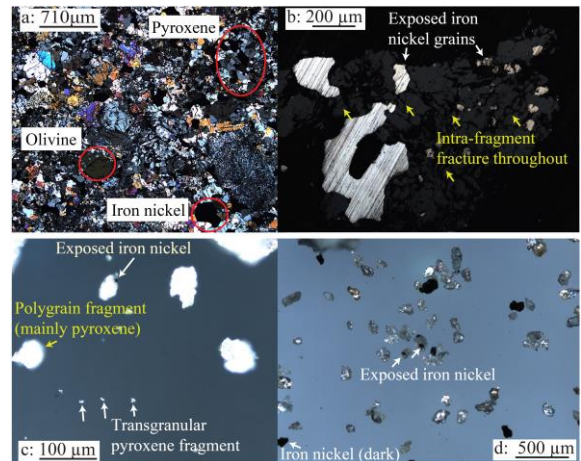


Fig. 1. (a) GRO 85209 thin section, (b) large and blocky polyphase fragment, (c) fragment character and (d) distribution of fractured grain in transmitted light.

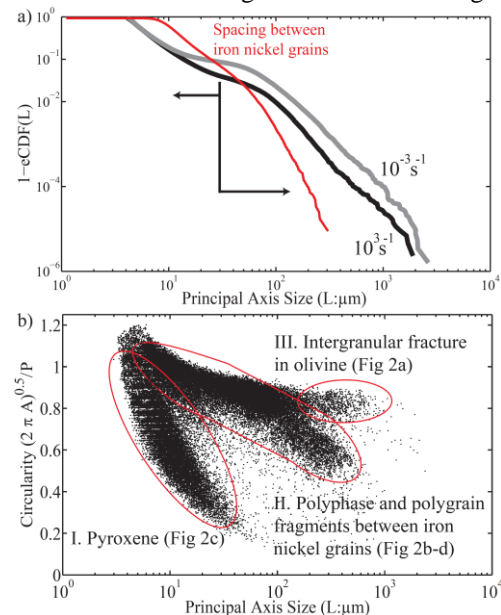


Fig. 2. (a) Cumulative distribution of meteorite fragments at 10^{-3} and 10^{+3} s^{-1} loading rates. Iron-nickel grain spacings is also included. (b) Circularity plotted against principal axis; note the three fragment regions.

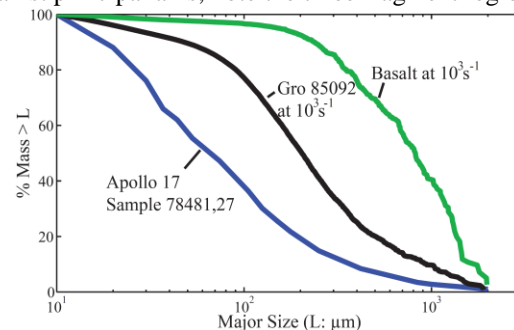


Fig. 3. Mass-size distributions for GRO 85029, basalt and lunar regolith sample 78481,27.